

Active Hyperspectral Imaging Using an Event Camera

Bohan Yu^{1,2†} Jinxiu Liang^{1,2} Zhuofeng Wang³
Bin Fan^{1,2} Art Subpa-asa⁴ Boxin Shi^{1,2*} Imari Sato⁴

¹ State Key Laboratory for Multimedia Information Processing, School of Computer Science, Peking University

² National Engineering Research Center of Visual Technology, School of Computer Science, Peking University

³ School of Electronics Engineering and Computer Science, Peking University ⁴ National Institute of Informatics

ybh1998@pku.edu.cn, cssherryliang@pku.edu.cn, wangzf2003@stu.pku.edu.cn,

binfan@pku.edu.cn, subpa@nii.ac.jp, shiboxin@pku.edu.cn, imarik@nii.ac.jp

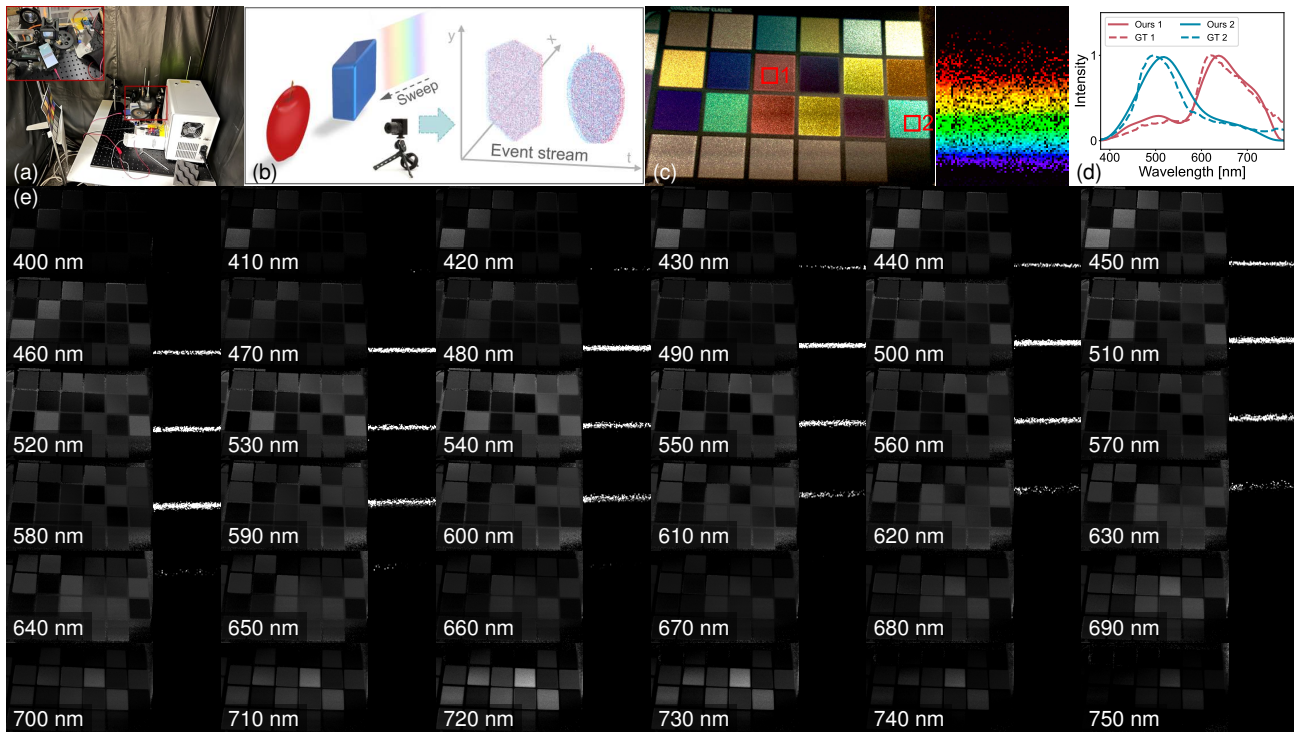


Figure 1. Our event-based active hyperspectral imaging system achieves real-time capture up to 30 FPS as well as 59.53% bandwidth reduction while maintaining accuracy comparable to frame-based methods. (a) System prototype. (b) Illustration of our working principle. (c) Reconstructed results in sRGB. (d) Spectral accuracy validation against ground truth. (e) Reconstructed hyperspectral images.

Abstract

Hyperspectral imaging plays a critical role in numerous scientific and industrial fields. Conventional hyperspectral imaging systems often struggle with the trade-off between capture speed, spectral resolution, and bandwidth, particu-

larly in dynamic environments. In this work, we present a novel event-based active hyperspectral imaging system designed for real-time capture with low bandwidth in dynamic scenes. By combining an event camera with a dynamic illumination strategy, our system achieves unprecedented temporal resolution while maintaining high spectral fidelity, all at a fraction of the bandwidth requirements of traditional systems. Unlike basis-based methods that sacrifice spectral resolution for efficiency, our approach enables con-

*Corresponding author: Boxin Shi

[†]This work was conducted while the first author, Bohan Yu, was doing internship at National Institute of Informatics.

tinuous spectral sampling through an innovative “sweeping rainbow” illumination pattern synchronized with a rotating mirror array. The key insight is leveraging the sparse, asynchronous nature of event cameras to encode spectral variations as temporal contrasts, effectively transforming the spectral reconstruction problem into a series of geometric constraints. Extensive evaluations of both synthetic and real data demonstrate that our system outperforms state-of-the-art methods in temporal resolution while maintaining competitive spectral reconstruction quality.

1. Introduction

Hyperspectral imaging, which captures detailed spectral information across a wide range of wavelengths, has become increasingly crucial in applications ranging from remote sensing [1, 14, 18] to medical diagnostics [5, 26, 50]. Traditional approaches typically suffer from a dilemma: they must balance spectral resolution, temporal resolution, and data bandwidth. While recent advances in computational imaging have made progress in addressing these challenges, existing solutions often require compromising among these competing factors. Specifically, current state-of-the-art methods broadly fall into three categories: *i)* scanning-based systems that achieve high spectral resolution at the cost of temporal resolution [4, 9, 10, 15, 21, 40], *ii)* snapshot systems that sacrifice spectral resolution for speed [31, 55, 59, 60], and *iii)* coded aperture approaches that require complex computational reconstruction [2, 22, 53]. Despite their respective merits, none of these approaches can simultaneously achieve high temporal resolution, high spectral resolution, and low bandwidth requirements—a capability increasingly demanded by emerging applications such as real-time material classification and dynamic scene understanding.

Event cameras have recently revolutionized high-speed imaging by responding to local intensity changes rather than capturing full frames, offering microsecond temporal resolution and high dynamic range [24, 35, 43]. They can potentially benefit real-time capture of hyperspectral imaging [16]. However, leveraging their advantages for hyperspectral imaging presents several fundamental challenges. *i)* Spectral information must be reliably encoded into temporal events while maintaining spatial consistency—a task complicated by motion artifacts and temporal aliasing in traditional scanning methods. *ii)* The sparse nature of events can exacerbate the ill-posedness of spectral reconstruction. *iii)* Event cameras’ inherent characteristics—logarithmic response, non-uniform pixel behavior, and refractory periods—introduce complex measurement inconsistencies.

In this paper, we propose an active hyperspectral imaging system using an event camera. Our key insight is that by synchronizing precisely controlled active illumination with an event camera’s superior temporal resolution, we

can encode spectral information in the temporal domain, effectively decoupling spectral resolution from temporal resolution. Specifically, our system includes a novel optical design that creates a “sweeping rainbow” effect through a synchronized rotating mirror array and blazed grating combination. An illustration of our system’s working principle using “sweeping rainbow” illumination to create temporal events encoding spectral information is shown in Fig. 1(b), where the scene contains objects with distinct single-peak spectral responses. This design integrates the cutting-edge features of event cameras, successfully transforming the complex problem of spectral reconstruction into a series of geometric constraints derived from event temporal information. Our mathematical framework shows that each event provides information about the underlying spectral distribution. Together with the usage of SVD and tailored constraints on the spectral solution, our method achieves robust reconstruction even with sparse temporal sampling and measurement inconsistencies in the event camera.

Our approach offers three fundamental advantages: *i)* microsecond-scale temporal resolution inherited from event cameras, enabling the capture of rapid spectral phenomena; *ii)* dramatic reduction in data bandwidth through sparse, asynchronous event representation; and *iii)* basis-independent spectral resolution, limited only by optical design rather than computational constraints. These make our method excel in applications demanding simultaneous high temporal and spectral resolution.

Our main technical contributions include:

- a novel active illumination strategy that enables continuous spectral sampling through precise synchronization with event-based sensing;
- a mathematical framework that reformulates the spectral reconstruction problem as a geometric constraint optimization problem; and
- an efficient solver that leverages physical prior derived from events for spectral reconstruction.

Through extensive experiments on both synthetic and real data, we demonstrate that our system achieves 59.53 % reduction in data bandwidth compared to traditional frame-based approaches. A comprehensive characterization of system performance and limitations is also conducted. Our approach enables the real-time capture (up to 30 FPS) of dynamic spectral phenomena with unconstrained spectral resolution, opening new possibilities in fields where real-time capture of spectral changes and minimal data bandwidth are essential.

2. Related Work

Hyperspectral imaging. Hyperspectral imaging systems have traditionally involved scanning the scene across either the spatial [4, 10, 40] or spectral [9, 15, 21] dimensions for passively capturing reflectance across different spectral

bands. Techniques such as spectral filters [41, 55], filter wheels [8], and tunable filters [9, 12, 15, 51] have been widely used to separate incoming light into distinct spectral components. However, these methods typically rely on sequential scanning, which significantly limits their temporal resolution and dynamic sensing capability, often leading to motion artifacts and spectral misalignment. Some methods leverage coded aperture [20, 45], disperser [2, 31], or both [22, 25, 53, 58–60] to form a Coded Aperture Snapshot Spectral Imaging (CASSI) system, achieving computational hyperspectral imaging from a subset of measurements. While offering faster acquisition speeds, they face challenges in terms of hardware complexity, versatility, and spectral accuracy. Moreover, researchers have explored alternative active illumination schemes [17, 23, 37, 46, 52, 54, 56] to reach a balance. Park *et al.* [37] showed multiplexed illumination could boost independent measurements using multiple light sources and camera channels. Similarly, Chi *et al.* [7] proposed optimized wide-band filtered illumination to maximize signal and minimize ambient light influence. Recently, Shin *et al.* [46] developed a hyperspectral imaging system based on dispersed structured light, utilizing a diffraction grating to achieve hyperspectral 3D imaging with higher spectral resolution than filter-based methods. The current landscape of hyperspectral imaging systems highlights the need for approaches that effectively address the inherent trade-offs between spectral resolution, temporal efficiency, and adaptability. Our proposed system extends previous works by combining active dispersive illumination with event-based imaging in a novel manner.

Event-based vision. Event cameras have reshaped imaging by enabling real-time data acquisition and robust performance in dynamic scenes. They can be used not only to directly reconstruct intensity videos [35, 36, 39, 42] or color videos [27, 30, 33, 44], but also to assist frame-based cameras in tasks like deblurring [48], high-frame-rate [49] and high-dynamic-range [29] imaging. Also, event cameras have improved deblurring in snapshot mosaic hyperspectral imaging [13]. In active lighting scenarios, event cameras capture rapid illumination shifts to enhance scene perception. Structured and intensity-varying lighting approaches trigger events for various applications. Structured lighting projects patterns onto objects, with event cameras capturing spatial disparities for 3D shape reconstruction [28]. High-speed digital light projection [19] facilitated 3D surface reconstruction through digital image correlation. ESL [34] synchronized projector and camera events, reducing noise in structured light applications. Besides structured light, researchers use light sources with intensity changes to trigger event signals. Morgenstern *et al.* [32] employed lookup tables for efficient real-time depth estimation under structure light. Takatani *et al.* [47] leveraged bispectral photometry under modulated light, enabling depth and concentration estimation in tur-

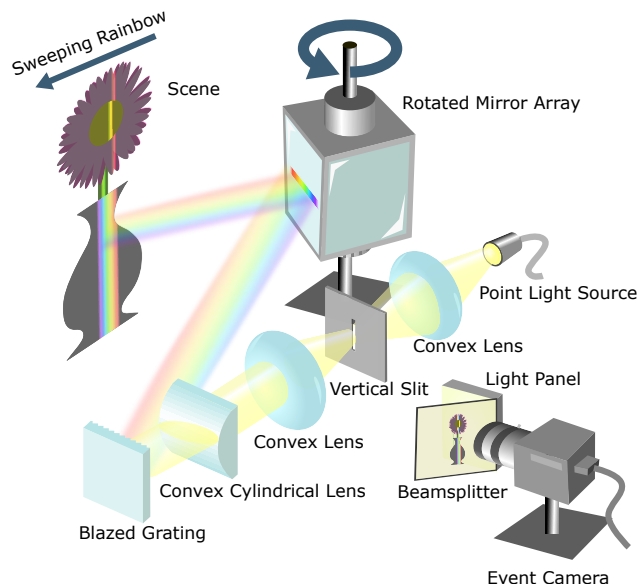


Figure 2. Illustration of our system. Our system combines a point light source, optical elements (convex lenses, vertical slit, and cylindrical lens), and a blazed grating to create a “sweeping rainbow” effect across the scene. The scattered light is collected through a beam-splitter and light panel arrangement before being captured by an event camera. This design enables rapid spectral scanning of the scene through the rotating mirror array’s continuous motion, whose temporal brightness changes are rapidly captured by the event camera with microsecond-level resolution.

bid media. EventPS [57] estimates the surface normal by analyzing the events triggered by a continuously rotating light source. Transient light triggers are employed [6, 16] to resolve intensity-distance ambiguity and capture radiance variations. Bajestani *et al.* [3] reconstructed color events with adaptive structured lighting, achieving an effective 1400 FPS with a monochrome event camera. Despite these advanced developments, active hyperspectral imaging with event cameras remains an unexplored area.

3. Method

3.1. Imaging Setup

Optical architecture. Our system adopts spectral decomposition to analyze different wavelengths of light from a scene, combining spatial scanning (via the rotating mirror array) with spectral separation (via the blazed grating) to build a complete hyperspectral data cube. Our system consists of three key components: a point light source with a convex lens for collimation, a rotating mirror array, and a blazed grating, synchronized for spectral separation. This configuration creates a “sweeping rainbow” effect that systematically maps spectral information to temporal variations. Fig. 1(a) shows the real capture prototype, and Fig. 2 shows how the optical path creates the spectral separation and how

the rotating mirror array facilitates the spatial scanning of the scene, with the rainbow pattern illustrating the spectral decomposition process.

The optical path begins with a collimated beam passing through a vertical slit, which is then directed through a series of convex and cylindrical lenses. This vertically parallel light interacts with the blazed grating, creating a wavelength-dependent angular dispersion. The rotating mirror array, positioned at the system's core, continuously redirects the dispersed light at precisely controlled angles. This process results in a temporally varying spectral illumination pattern that dynamically sweeps across the scene.

Temporal-spectral encoding. The key insight of our design is that the rotating mirror array creates a deterministic illumination pattern, which establishes the relationship between wavelength λ and time τ . For a pixel x, y in the scene, the incoming spectral radiance $L_{x,y}(\lambda, \tau)$ from our illumination device is a function as follows:

$$L_{x,y}(\lambda, \tau) = T(\lambda + \beta\omega(\tau + \hat{\tau}_x)), \quad (1)$$

where T is the spectral radiance of the narrow-band dispersed light, ω is the illumination pattern rotation speed (half of the mirror rotation speed), $\hat{\tau}_x$ is the initial time offset depending on the horizontal coordinate of the pixel, and β is a coefficient describing the width of the rainbow in the unit of nanometer per rad. This relationship enables us to encode high-dimensional spectral information into a temporal sequence that can be efficiently captured by an event camera.

3.2. Problem Formation

Event formation model. Event cameras capture scene radiance changes on a logarithmic scale. Each pixel measures the radiance changes asynchronously. When the changes of logarithmic radiance at the pixel x, y reaches a triggering threshold C , an event $\{x, y, \sigma, \tau\}$ will be triggered, where τ is the timestamp, and $\sigma \in \{-1, +1\}$ is the polarity representing the decrease or increase of radiance. Assume there are totally K events triggered at pixel x, y during an illumination cycle. These events are represented as $\mathcal{E}_{x,y} = \{x, y, \sigma_k, \tau_k\}$, where $k = \{1, 2, \dots, K\}$. The change of radiance value in pixel x, y from τ_{k-1} to τ_k becomes:

$$\log(I_{x,y}(\tau_k) + \epsilon) = \log(I_{x,y}(\tau_{k-1} + \eta) + \epsilon) + \sigma_k C, \quad (2)$$

where ϵ is a small offset value to avoid taking the logarithm of zero, and η is the refractory time of the pixel [11]. In our system, these intensity changes are induced by the sweeping spectral illumination. Combining the event generation model with our spectral illumination pattern, we can express the relationship between events and spectral content.

Hyperspectral imaging model. Assuming that there is an object illuminated by an ideal white point light source, which exhibits a flat spectrum curve in the visible light range. For a pixel x, y under spectrum λ , the hyperspectral image pixel

intensity $S_{x,y}(\lambda)$ has the following formula:

$$S_{x,y}(\lambda) = R_{x,y}(\lambda)E(\lambda), \quad (3)$$

where $R_{x,y}(\lambda)$ is the reflectance of pixel x, y , and $E(\lambda)$ is the spectral radiance of the ideal white light source shared by all the image plane. Here we assume that the material is non-fluorescent to allow each spectrum be treated independently, omit inter-reflection and sub-surface scattering to have each pixel be treated independently.

To capture spectrally relevant information using a monochromatic event camera, we design the illumination pattern $L_{x,y}(\lambda, \tau)$ that varies along both wavelength and time as shown in Eq. (1). For a pixel x, y , the observed intensity $I_{x,y}(\tau)$ at time τ is determined by the interaction between the scene's spectral reflectance and our time-varying illumination $L_{x,y}(\lambda, \tau)$ as follows:

$$\begin{aligned} I_{x,y}(\tau) &= \int_{\lambda} D(\lambda)R_{x,y}(\lambda)L_{x,y}(\lambda, \tau)d\lambda \\ &= \int_{\lambda} D(\lambda)S_{x,y}(\lambda)\frac{L_{x,y}(\lambda, \tau)}{E(\lambda)}d\lambda, \end{aligned} \quad (4)$$

where $D(\lambda)$ denotes the camera spectral response curve shared by all positions, and $S_{x,y}(\lambda)$ represents the hyper-spectral image, which is our reconstruction target.

Therefore, the event-based active hyperspectral imaging estimation task can be formalized as: by designing the changing light source function $L_{x,y}(\lambda, \tau)$, given the events captured by an event camera, estimate the hyperspectral image $S_{x,y}(\lambda)$ as if it is illuminated by an ideal white point light source.

3.3. Event-Based Spectral Reconstruction

In order to estimate the continuous hyper-spectrum image function $S_{x,y}(\lambda)$ in a numerical way, the continuous equation should be discretized for practical implementation. Specifically, we separate the spectral response over the visible spectrum into a discrete set $\mathbb{S} = [\lambda_1, \lambda_2, \dots, \lambda_M]$ of M centered wavelengths sampled from 400 nm to 760 nm with $\delta = \frac{360}{M}$ nm interval. Then we can rewrite Eq. (4) into a discrete form:

$$I_{x,y}(\tau) = \sum_m S_{x,y,m} \int_{\lambda_m}^{\lambda_m + \delta} D(\lambda)\frac{L_{x,y}(\lambda, \tau)}{E(\lambda)}d\lambda. \quad (5)$$

Denote the right part that can be pre-calibrated as:

$$A_{x,y,m}(\tau) = \int_{\lambda_m}^{\lambda_m + \delta} D(\lambda)\frac{L_{x,y}(\lambda, \tau)}{E(\lambda)}d\lambda, \quad (6)$$

then we have

$$I_{x,y}(\tau) = \sum_m A_{x,y,m}(\tau)S_{x,y,m} \quad (7)$$

For the sake of simplicity, we convert the M dimension of $S_{x,y,m}$ and $A_{x,y,m}(\tau)$ into vectors $\mathbf{x} \in \mathbb{R}^M$ and $\mathbf{a}_\tau \in \mathbb{R}^M$. Also, we only focus on one pixel and omit the subscript x, y in the following sections. The problem can be simplified

using the dot product

$$I(\tau) = \mathbf{a}_\tau \cdot \mathbf{x}, \quad (8)$$

at each pixel x, y and moment τ .

Null spectrum vector for spectral-temporal mapping. Recall that for each pixel x, y , events are triggered when logarithmic intensity changes exceed threshold C . To see what each pair of events reveals about the hyper-spectrum image, we combine Eq. (8) with Eq. (2) (omitting the non-ideal bias and refractory time) to get the following equation for each pair of events triggered at timestamps τ_k, τ_{k-1} :

$$\mathbf{a}_{\tau_k} \cdot \mathbf{x} = e^{C\sigma_k} \mathbf{a}_{\tau_{k-1}} \cdot \mathbf{x}. \quad (9)$$

We denote all the components besides \mathbf{x} as follows:

$$\mathbf{n}_k = \mathbf{a}_{\tau_k} - e^{C\sigma_k} \mathbf{a}_{\tau_{k-1}}. \quad (10)$$

All the components in \mathbf{n}_k are either calibrated in advance, or extracted from the event stream. Then we can see that $\mathbf{n}_k \in \mathbb{R}^M$ is perpendicular to \mathbf{x} because their dot product is 0, i.e.,

$$\mathbf{n}_k \cdot \mathbf{x} = 0. \quad (11)$$

Here, we name the vector \mathbf{n}_k as *null spectrum vector*.

The event-triggered constraints provide a series of equations Eq. (9) that relate consecutive measurements. Each pair of events generates a null spectrum vector $\hat{\mathbf{n}}_k$ according to equation Eq. (10), forming the basis of our reconstruction approach.

Spectral reconstruction from augmented null spectrum vectors. Null spectrum vector provides information about the spectrum shape of the target image $S(\lambda)$. However, the absolute value of the image is still ambiguous. To solve this problem, we add a direct light to the sensor and propose the following augmented null spectrum vector.

The event signal captured previously lacks absolute intensity because the event only provides a relative intensity ratio between a pair of timestamps. To introduce the absolute intensity value into the event signal, we add a constant intensity value c to the sensor. This addition is achieved by putting a beam splitter and another constant planner light in front of the event camera. The captured intensity $\hat{I}(\tau)$ with this constant light has the following formula:

$$\hat{I}(\tau) = \mathbf{a}_\tau \cdot \mathbf{x} + c = \begin{bmatrix} \mathbf{x} \\ 1 \end{bmatrix} \cdot \begin{bmatrix} \mathbf{a}_\tau \\ c \end{bmatrix}. \quad (12)$$

By concatenating another dimension with the added constant light intensity c , we achieve the augmented null spectrum vector $\hat{\mathbf{n}}_k$ as:

$$\hat{\mathbf{x}} \cdot \hat{\mathbf{n}}_k = 0, \quad (13)$$

where

$$\hat{\mathbf{x}} = \begin{bmatrix} \mathbf{x} \\ 1 \end{bmatrix}, \quad \text{and} \quad \hat{\mathbf{n}}_k = \begin{bmatrix} \mathbf{a}_k \\ c \end{bmatrix} - e^{\sigma_k C} \begin{bmatrix} \mathbf{a}_{k-1} \\ c \end{bmatrix}. \quad (14)$$

The events $\mathcal{E}_{x,y}$ triggered at pixel x, y over time within the static state of the scene can build up a system of constraints.

Denote matrix $\hat{\mathbf{N}} \in \mathbb{R}^{K \times (M+1)}$ the matrix whose rows are $M+1$ dimensional augmented null spectrum vectors $\hat{\mathbf{n}}_k, k = 1, 2, \dots, K$. We can calculate \mathbf{x} by solving the least square minimization problem

$$\mathbf{x}^* = \operatorname{argmin}_{\mathbf{x}} \|\hat{\mathbf{N}}\hat{\mathbf{x}}\|_2. \quad (15)$$

The weight of hyper-spectrum image \mathbf{x} can be calculated by performing SVD, selecting the singular vector corresponding to the minimum singular value, and normalizing it according to the last dimension. However, there are three problems if deploying the SVD solution directly:

- The SVD solution contains negative values, while all intensities should be positive. The SVD method tends to form a zero-crossing point around frequent events to reduce overall error. As a result, solutions containing zero-crossing points are mostly all wrong.
- The augmented null spectrum vectors $\hat{\mathbf{n}}_k$ only provide relative intensity relations among event triggering timestamps. When there is a long gap between the event triggering time, there are no restrictions for the intensity value between the two endpoint timestamps. Drastically changing intensity between the gaps violates the event triggering model.
- For dark pixels or pixels with flat spectrum (white color). There are fewer events generated than the number of bases. The matrix from augmented null spectrum vectors $\hat{\mathbf{n}}_k$ is degraded, and there are infinite solutions in this case.

To solve the first SVD negative value problem, we introduce another set of inequality constraints $S(\lambda) \geq 0, \forall \lambda$, which can be written as:

$$\mathbf{x}_m \geq 0, \quad m = 1, 2, \dots, M \quad (16)$$

which convert the linear least square minimization problem Eq. (15) into a quadratic programming (QP) problem.

To solve the second long-event-gap hallucinations problem, we introduce a regularization term to suppress drastic intensity drift in the gap of a pair of events. This regularization term adds an L2 penalty to the intensity values between two events and the linear interpolation between each pair of events as follows:

$$R_{\text{int}} = \sum_k \sum_{\tau \in (\tau_{k-1}, \tau_k)} ((\mathbf{a}_\tau - \mathbf{a}'_\tau) \cdot \mathbf{x})^2, \quad (17)$$

where

$$\mathbf{a}'_\tau = \frac{\tau_k - \tau}{\tau_k - \tau_{k-1}} \mathbf{a}_{\tau_{k-1}} + \frac{\tau - \tau_{k-1}}{\tau_k - \tau_{k-1}} \mathbf{a}_{\tau_k}. \quad (18)$$

To solve the third matrix degraded problem, we introduce another regularization term to suppress high-frequency changes in the spectrum as follows:

$$R_{\text{spec}} = \sum_{k \in [M_{\text{start}}, M]} (\mathbf{f}_k \cdot \mathbf{x})^2, \quad (19)$$

where $\mathbf{f}_k = \left[\cos \frac{1.5k\pi}{M}, \cos \frac{2.5k\pi}{M}, \dots, \cos \frac{k\pi(M+0.5)}{M} \right]^\top$, and M_{start} represents the frequency to start adding penalty.

To summarize, given a set of events at pixel x, y over time,

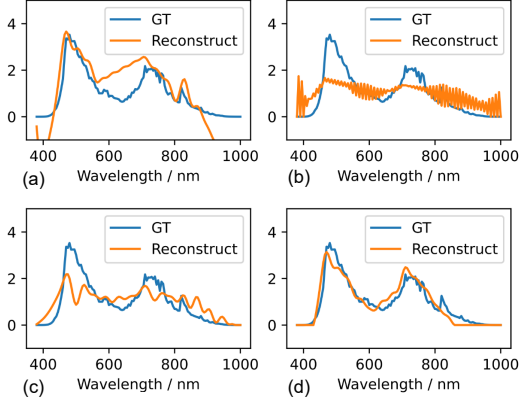


Figure 3. Influence of different constraints on spectral reconstruction quality. Four variants are compared: (a) without non-negative constraints, showing physically implausible negative spectral values (SAM: 30.23, PSNR: 26.62); (b) without low-frequency prior, resulting in high-frequency artifacts (SAM: 30.97, PSNR: 26.42); (c) with reduced anti-drift constraints, exhibiting temporal instability (SAM: 26.28, PSNR: 27.81); and (d) our full method incorporating all constraints, achieving the most accurate and stable reconstruction (SAM: 13.42, PSNR: 33.60).

the spectral reconstruction in Eq. (15) can be reformulated as a constrained optimization problem:

$$\min_{\mathbf{x}} \left(\|\tilde{\mathbf{N}}\hat{\mathbf{x}}\|_2^2 + \alpha_{\text{int}}R_{\text{int}}(\mathbf{x}) + \alpha_{\text{spec}}R_{\text{spec}}(\mathbf{x}) \right), \quad (20)$$

subject to : $\mathbf{x}_m \geq 0, \quad m = 1, 2, \dots, M,$

where $R_{\text{int}}(\mathbf{x})$ is a sparsity regularizer addressing measurement noise, $R_{\text{spec}}(\mathbf{x})$ is a smoothness regularizer promoting spectral continuity, $\alpha_{\text{int}}, \alpha_{\text{spec}}$ are regularization parameters.

Fig. 3 illustrates the critical role of different constraints in our reconstruction pipeline. The ablation study demonstrates that non-negative constraints prevent physically impossible negative spectral values, while low-frequency priors suppress high-frequency artifacts. Anti-drift constraints ensure temporal stability.

3.4. Calibration

Calibration is crucial for reliable hyperspectral reconstruction. Our system requires the calibration of several parameters: the time-varying spectral intensity of the sweeping rainbow illumination $L(\lambda, \tau)$, the constant illumination c , the event camera’s spectral response curve $D(\lambda)$, and the event triggering threshold C . A detailed description of the calibration procedure of c , $D(\lambda)$, and C can be found in the supplementary, while the calibration of $L(\lambda, \tau)$ is as follows.

We decompose the calibration of $L(\lambda, \tau)$ into two sub-problems using a laser point as a temporal-spatial reference. The laser beam, being reflected by the same mirror array, maintains a fixed relative position to the sweeping rainbow strip. First, the temporal relationship between the rainbow strip arrival and event triggering at each pixel is established.

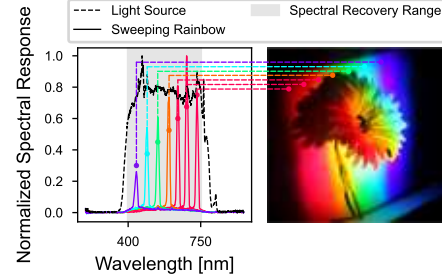


Figure 4. Temporal evolution of spectral illumination patterns of our system. Different narrow-band illuminations are projected to different locations of the scene, forming a sweeping rainbow strip pattern. Spectral characteristics of the broadband light source and reconstructed hyper-spectral imaging range are also elaborated.

Assuming vertical alignment of the projected rainbow strip, pixels in the same column experience identical temporal patterns. We track the laser point position at the scene’s bottom edge to determine these temporal relationships. Second, we characterize the spectral intensity distribution across time by operating the mirror array at a constant, low angular velocity while recording spectral measurements with a spectrometer. By modulating the laser between on and off during measurement and correlating with detected laser positions, we obtain a comprehensive mapping of spectral intensity variations across both time and wavelength. The real-world spectral radiance captured from our modulated illumination pattern is shown in Fig. 4, along with the input lamp spectral radiance and the position mapping to the rainbow strip.

4. Experiments

4.1. Implementation Details

Our prototype system employs an IMX636 event camera as the primary sensor. Illumination is provided by a high-power xenon lamp, which delivers the broad spectral coverage and intensity stability necessary for reliable hyperspectral measurements. To establish a stable baseline illumination level, we utilize an iPhone 7’s LCD display with DC dimming capability, eliminating potential temporal artifacts from screen flicker. The rotating mirror array operates at two distinct speeds: 180 rpm for static scene capture, and 600 rpm for dynamic scenes, enabling hyperspectral video capture at 10 frames per second. Our spectral reconstruction pipeline estimates 72 discrete channels spanning 400 – 760 nm at 5 nm intervals, providing detailed coverage of the visible spectrum. Details of the algorithm are in the supplementary.

4.2. Experimental Protocol

Ground truth acquisition. Ground truth spectral measurements are obtained using a calibrated EBA NH8 hyperspectral camera, capable of measuring spectra from 380-1000 nm. These measurements are conducted under the same xenon

lamp used in our system, allowing direct calculation of surface reflectance spectra for validation. The measurements are spatially registered with our reconstructions.

Data simulation. Our synthetic dataset generation pipeline simulates the complete optical and sensing characteristics of the system, including the non-ideal narrow-band illumination pattern, non-ideal event triggering, and frame camera imaging noises. More details can be found in the supplementary material.

Compared methods. We evaluate the proposed system against the following baselines: *i*) Full-bandwidth frame-based method. *ii*) Bandwidth-matched frame-based method. *iii*) Parkkinen basis method [38]. *iiii*) CASSI-based method [25, 58]. More details can be found in the supplementary material.

4.3. Comparison Results

High-frequency spectral feature recovery. We first evaluate our method’s capability to recover high-frequency spectral features using a challenging rainbow pattern (Fig. 5). This test case is particularly demanding as it contains sharp spectral transitions and narrow-band features that are difficult to capture with traditional methods. As shown in Fig. 5(a-d), basis-based methods struggle to accurately represent these sharp spectral features, exhibiting significant smoothing artifacts. While the full-bandwidth frame-based method (1200 frames) captures these features accurately, it requires substantial data bandwidth, 100 times compared to ours. The bandwidth-matched frame-based method, operating under the same data constraints as our approach, shows degraded performance due to temporal undersampling. Our method (Fig. 5(b)) successfully recovers the sharp spectral transitions while maintaining high spatial fidelity. The spectral profiles in Fig. 5(i) demonstrate that our approach achieves acceptable accuracy using significantly low bandwidth. This superior performance stems from our event-based encoding scheme, which efficiently captures temporal changes in spectral information.

We also compare our method with CASSI-based methods [25, 58] and evaluate the event efficiency comparing frame-based methods with our method. More details can be found in the supplementary material.

4.4. Evaluation on Synthetic Data

Evaluation on a ColorChecker. We conduct a systematic evaluation using a standard ColorChecker chart (Fig. 6), which provides a diverse set of well-characterized spectral signatures. The quantitative results show that our method achieves an RMS error of 0.204, SAM of 21.05, and PSNR of 28.46 on average across all 24 patches, with particularly strong performance in regions of smooth spectral variation. The reconstructed spectra (Fig. 6, bottom) demonstrate our method’s ability to accurately recover both broad and nar-

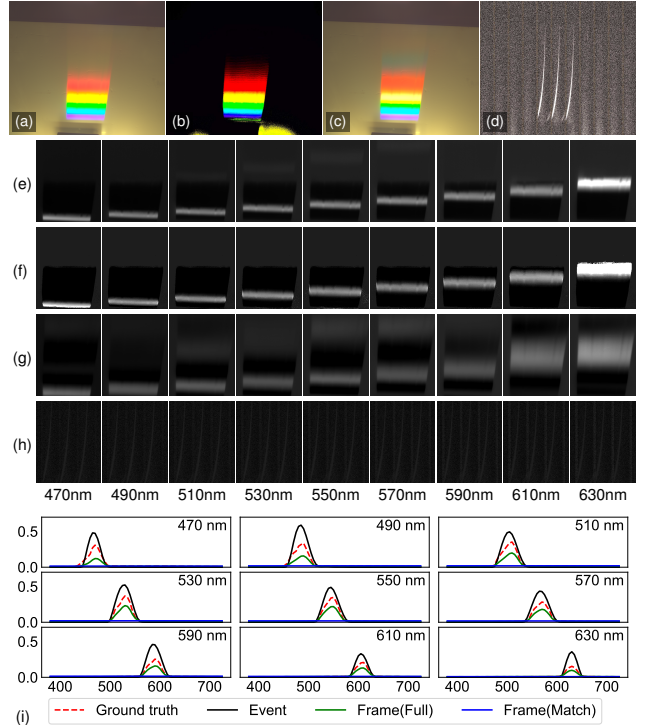


Figure 5. Comparative analysis of spectral reconstruction on a high-frequency rainbow pattern. Compared methods include (a) ground truth, (b) ours (SAM: 23.27, PSNR: 24.61, SSIM: 0.40), (c) basis-based method (SAM: 25.97, PSNR: 23.79, SSIM: 0.68), (d) bandwidth-matched frame-based method (SAM: NaN, PSNR: 18.73, SSIM: 0.14), with corresponding hyperspectral visualizations (e-h). Spectral profiles (i) validate our method’s superior performance over the bandwidth-full and bandwidth-matched frame-based method.

row spectral features. The error analysis reveals that our approach maintains consistent accuracy across different spectral patterns, with slightly higher uncertainty in regions of flat spectral curves.

Evaluation on metameric samples. To evaluate our system’s ability to distinguish subtle spectral differences, we analyze metameric samples of real and fake daisies (Fig. 7). Our method successfully captures the subtle spectral differences between the metameric pairs (Fig. 7(b)), demonstrating sensitivity to fine spectral features that are crucial for material classification applications. The full hyperspectral reconstruction (Fig. 7(c)) shows consistent performance across the entire spatial field.

4.5. Evaluation on Real Data

Evaluation on static scene. The real-world performance of our system is demonstrated through comprehensive static scene captures (Fig. 1). Our prototype achieves 59.53% bandwidth reduction compared to traditional frame-based systems while maintaining comparable accuracy (Fig. 1(d)). The reconstructed hyperspectral images (Fig. 1(c,e)) show

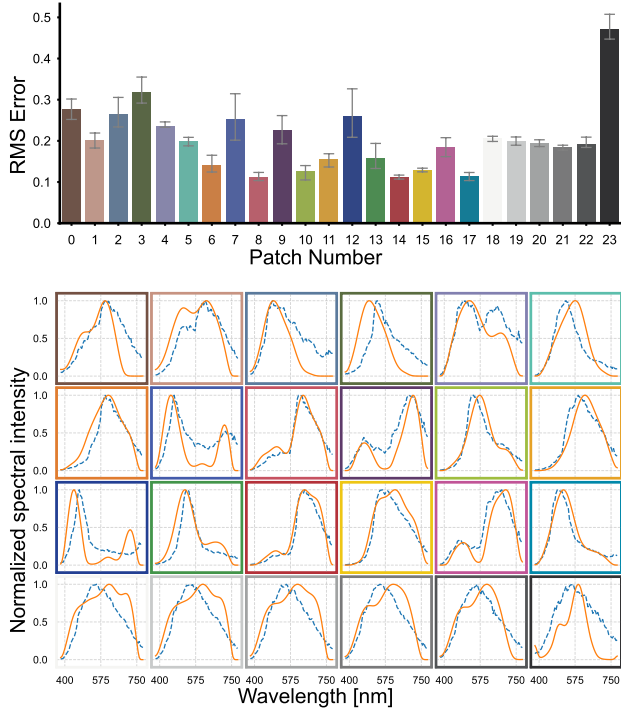


Figure 6. Evaluation on a ColorChecker. Our method achieves 21.05 SAM and 28.46 PSNR on average across all 24 patches. Top: Spectral accuracy evaluation in terms of RMS error and error bar from 14 measurements, where 2,500 pixels are used in evaluation for each patch. The blue column indicates the mean RMS error. Bottom: Reconstructed spectra of all 24 patches, where solid lines are ours, and the dashed lines are ground truth.

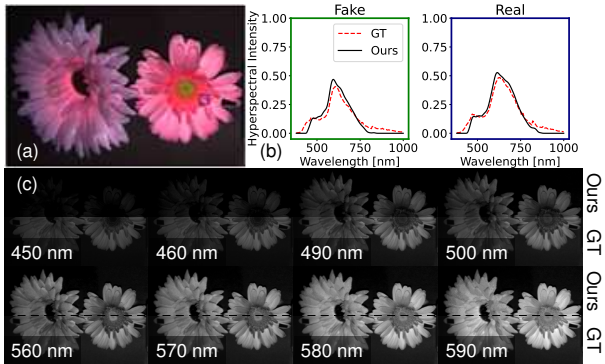


Figure 7. Evaluation on metameric samples of fake (left) and real (right) daisies. Our method achieves 10.8 SAM and 34.95 PSNR on average. (a) The reconstructed hyperspectral image in sRGB. (b) Spectra of metameric samples against ground truth measurements, highlighting the system’s ability to capture subtle spectral differences. (c) Estimated hyperspectral images.

excellent agreement with ground truth measurements at representative points.

Evaluation on dynamic scene. A key advantage of our approach is its ability to capture dynamic spectral phenomena. Fig. 8 demonstrates this capability through the capture of an iridescent paper in motion. The system achieves a tem-

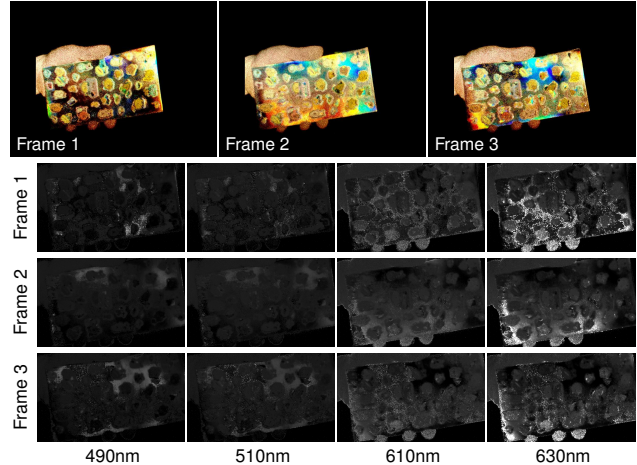


Figure 8. Real-time hyperspectral imaging on a moving iridescent sticker paper. Top: Three consecutive estimated hyperspectral images rendered in sRGB captured within 0.3 s. Bottom: Corresponding estimated hyperspectral images.

poral resolution of 10 FPS while maintaining high spectral fidelity, enabling the observation of rapid spectral changes that would be impossible to capture with traditional systems.

5. Conclusion

In this paper, we present the first event-based hyperspectral imaging system. By encoding spectral data through temporal contrast, our approach leverages the sparse, asynchronous nature of event cameras to achieve dramatic bandwidth reductions while maintaining high spectral and temporal resolution. The system demonstrates that breaking the resolution-bandwidth trade-off is possible through careful co-design of optical hardware and computational algorithms. Experimental results demonstrate that our approach enables real-time capture of dynamic spectral phenomena with unconstrained spectral resolution, achieving performance comparable to frame-based methods with only 40.47% of the data.

Limitations. Currently, the inter-reflection, scattering, and fluorescence of the material are not modeled. They will affect spectral estimation accuracy. The system requires precise optical calibration and the algorithm implementation still has room to speed up. Future work could address these limitations by improving optical systems or introducing deep learning techniques.

Acknowledgement

This work is supported by National Natural Science Foundation of China (Grant No. 624B2006, 62088102, 62136001, 62302019), Beijing Natural Science Foundation (Grant No. L233024), JST-Mirai Program (Grant No. JPMJM123G1), and JSPS Kakenhi (Grant No. 20H05953). PKU-affiliated authors thank openbayes.com for providing computing resource.

References

- [1] Telmo Adão, Jonáš Hruška, Luís Pádua, José Bessa, Emanuel Peres, Raul Morais, and Joaquim Joao Sousa. Hyperspectral imaging: A review on uav-based sensors, data processing and applications for agriculture and forestry. *Remote Sensing*, 9(11):1110, 2017. 2
- [2] Seung-Hwan Baek, Incheol Kim, Diego Gutierrez, and Min H Kim. Compact single-shot hyperspectral imaging using a prism. *ACM Transactions on Graphics*, 36(6):1–12, 2017. 2, 3
- [3] Seyed Ehsan Marjani Bajestani and Giovanni Beltrame. Event-based rgb sensing with structured light. In *Proc. of IEEE/CVF Winter Conference on Applications of Computer Vision*, pages 5447–5456, 2023. 3
- [4] Robert W Basedow, Dwayne C Carmer, and Mark E Anderson. Hydice system: Implementation and performance. In *Imaging Spectrometry*, pages 258–267, 1995. 2
- [5] Mihaela Antonina Calin, Sorin Viorel Parasca, Dan Savastru, and Dragos Manea. Hyperspectral imaging in the medical field: Present and future. *Applied Spectroscopy Reviews*, 49(6):435–447, 2014. 2
- [6] Zehao Chen, Qian Zheng, Peisong Niu, Huajin Tang, and Gang Pan. Indoor lighting estimation using an event camera. In *Proc. of Computer Vision and Pattern Recognition*, pages 14760–14770, 2021. 3
- [7] Cui Chi, Hyunjin Yoo, and Moshe Ben-Ezra. Multi-spectral imaging by optimized wide band illumination. *International Journal of Computer Vision*, 86(2):140, 2008. 3
- [8] Jason M Eichenholz, Nick Barnett, and Dave Fish. Sequential filter wheel multispectral imaging systems. In *Applied Industrial Optics: Spectroscopy, Imaging and Metrology*, page ATuB2, 2010. 3
- [9] Jianan Fang, Kun Huang, Ruiyang Qin, Yan Liang, E Wu, Ming Yan, and Heping Zeng. Wide-field mid-infrared hyperspectral imaging beyond video rate. *Nature Communications*, 15(1):1811, 2024. 2, 3
- [10] James E Fowler. Compressive pushbroom and whiskbroom sensing for hyperspectral remote-sensing imaging. In *Proc. of International Conference on Image Processing*, pages 684–688, 2014. 2
- [11] Guillermo Gallego, Tobi Delbrück, Garrick Orchard, Chiara Bartolozzi, Brian Taba, Andrea Censi, Stefan Leutenegger, Andrew J Davison, Jörg Conradt, Kostas Daniilidis, et al. Event-based vision: A survey. *IEEE Transactions on Pattern Analysis and Machine Intelligence*, 44(1):154–180, 2020. 4
- [12] Nahum Gat. Imaging spectroscopy using tunable filters: A review. *Wavelet Applications VII*, 4056:50–64, 2000. 3
- [13] Mengyue Geng, Lizhi Wang, Lin Zhu, Wei Zhang, Ruiqin Xiong, and Yonghong Tian. Event-enhanced snapshot mosaic hyperspectral frame deblurring. *IEEE Transactions on Pattern Analysis and Machine Intelligence*, pages 1–18, 2024. 3
- [14] Ying Guo, Bin Fan, Yan Feng, Xiuping Jia, and Mingyi He. Distribution-aware and class-adaptive aggregation for few-shot hyperspectral image classification. *IEEE Transactions on Geoscience and Remote Sensing*, 62:1–16, 2024. 2
- [15] Neelam Gupta, Rachid Dahmani, and Steve Choy. Acousto-optic tunable filter based visible-to near-infrared spectropolarimetric imager. *Optical Engineering*, 41(5):1033–1038, 2002. 2, 3
- [16] Jin Han, Yuta Asano, Boxin Shi, Yinqiang Zheng, and Imari Sato. High-fidelity event-radiance recovery via transient event frequency. In *Proc. of Computer Vision and Pattern Recognition*, pages 20616–20625, 2023. 2, 3
- [17] Shuai Han, Imari Sato, Takahiro Okabe, and Yoichi Sato. Fast spectral reflectance recovery using DLP projector. *International Journal of Computer Vision*, 110:172–184, 2014. 3
- [18] Danfeng Hong, Zhu Han, Jing Yao, Lianru Gao, Bing Zhang, Antonio Plaza, and Jocelyn Chanussot. SpectralFormer: Rethinking hyperspectral image classification with transformers. *IEEE Transactions on Geoscience and Remote Sensing*, 60:1–15, 2021. 2
- [19] Xueyan Huang, Yueyi Zhang, and Zhiwei Xiong. High-speed structured light based 3D scanning using an event camera. *Optics Express*, 29(22):35864–35876, 2021. 3
- [20] Daniel S. Jeon, Seung-Hwan Baek, Shinyoung Yi, Qiang Fu, Xiong Dun, Wolfgang Heidrich, and Min H. Kim. Compact snapshot hyperspectral imaging with diffracted rotation. *ACM Trans. Graph.*, 38(4), 2019. 3
- [21] David B Kelley, Anish K Goyal, Ninghui Zhu, Derek A Wood, Travis R Myers, Petros Kotidis, Cara Murphy, Chelsea Georgian, Gil Raz, Richard Maulini, et al. High-speed mid-infrared hyperspectral imaging using quantum cascade lasers. In *Chemical, Biological, Radiological, Nuclear, and Explosives (CBRNE) Sensing XVIII*, pages 19–28, 2017. 2
- [22] Kareth M León-López, Laura V Galvis Carreno, and Henry Arguello Fuentes. Temporal colored coded aperture design in compressive spectral video sensing. *IEEE Transactions on Image Processing*, 28(1):253–264, 2018. 2, 3
- [23] Chunyu Li, Yusuke Monno, Hironori Hidaka, and Masatoshi Okutomi. Pro-cam ssm: Projector-camera system for structure and spectral reflectance from motion. In *Proc. of International Conference on Computer Vision*, pages 2414–2423, 2019. 3
- [24] Jinxiu Liang, Yixin Yang, Boyu Li, Peiqi Duan, Yong Xu, and Boxin Shi. Coherent event guided low-light video enhancement. In *Proc. of International Conference on Computer Vision*, 2023. 2
- [25] Yang Liu, Xin Yuan, Jinli Suo, David J. Brady, and Qionghai Dai. Rank minimization for snapshot compressive imaging. *IEEE Trans. Pattern Anal. Mach. Intell.*, 41(12):2990 – 3006, 2019. 3, 7
- [26] Harshita Mangotra, Sahima Srivastava, Garima Jaiswal, Ritu Rani, and Arun Sharma. Hyperspectral imaging for early diagnosis of diseases: A review. *Expert Systems*, 40(8):e13311, 2023. 2
- [27] Alexandre Marcireau, Sio-Hoi Ieng, Camille Simon-Chane, and Ryad B. Benosman. Event-based color segmentation with a high dynamic range sensor. *Frontiers in Neuroscience*, 12, 2018. 3
- [28] Nathan Matsuda, Oliver Cossairt, and Mohit Gupta. MC3D: Motion contrast 3D scanning. In *Proc. of International Conference on Computational Photography*, pages 1–10, 2015. 3

- [29] Nico Messikommer, Stamatios Georgoulis, Daniel Gehrig, Stepan Tulyakov, Julius Erbach, Alfredo Bochicchio, Yuanyou Li, and Davide Scaramuzza. Multi-bracket high dynamic range imaging with event cameras. In *Proc. of Computer Vision and Pattern Recognition Workshops*, pages 547–557, 2022. 3
- [30] Diederik Paul Moeys, Chenghan Li, Julien N.P. Martel, Simeon Bamford, Luca Longinotti, Vasyl Motsnyi, David San Segundo Bello, and Tobi Delbruck. Color temporal contrast sensitivity in dynamic vision sensors. In *Pro. of IEEE International Symposium on Circuits and Systems*, pages 1–4, 2017. 3
- [31] Kristina Monakhova, Kyrollos Yanny, Neerja Aggarwal, and Laura Waller. Spectral DiffuserCam: lensless snapshot hyperspectral imaging with a spectral filter array. *Optica*, 7(10):1298–1307, 2020. 2, 3
- [32] Wieland Morgenstern, Niklas Gard, Simon Baumann, Anna Hilsmann, and Peter Eisert. X-Maps: Direct depth lookup for event-based structured light systems. In *Proc. of Computer Vision and Pattern Recognition*, pages 4007–4015, 2023. 3
- [33] Mohammad Mostafavi, Lin Wang, and Kuk-Jin Yoon. Learning to reconstruct HDR images from events, with applications to depth and flow prediction. *International Journal of Computer Vision*, 129(4):900–920, 2021. 3
- [34] Manasi Muglikar, Guillermo Gallego, and Davide Scaramuzza. ESL: Event-based structured light. In *Proc. of International Conference on 3D Vision*, pages 1165–1174, 2021. 3
- [35] Gottfried Munda, Christian Reinbacher, and Thomas Pock. Real-time intensity-image reconstruction for event cameras using manifold regularisation. *International Journal of Computer Vision*, 126(12):1381–1393, 2018. 2, 3
- [36] Liyuan Pan, Cedric Scheerlinck, Xin Yu, Richard Hartley, Miaomiao Liu, and Yuchao Dai. Bringing a blurry frame alive at high frame-rate with an event camera. In *Proc. of Computer Vision and Pattern Recognition*, pages 6820–6829, 2019. 3
- [37] Jong-Il Park, Moon-Hyun Lee, Michael D. Grossberg, and Shree K. Nayar. Multispectral imaging using multiplexed illumination. In *Proc. of International Conference on Computer Vision*, pages 1–8, 2007. 3
- [38] J. P. S. Parkkinen, J. Hallikainen, and T. Jaaskelainen. Characteristic spectra of Munsell colors. *JOSA A*, 6(2):318–322, 1989. 7, 3
- [39] Henri Rebecq, Rene Ranftl, Vladlen Koltun, and Davide Scaramuzza. Events-to-video: Bringing modern computer vision to event cameras. In *Proc. of Computer Vision and Pattern Recognition*, pages 3857–3866, 2019. 3
- [40] Lee J Rickard, Robert W Basedow, Edward F Zalewski, Peter R Silverglate, and Mark Landers. HYDICE: An airborne system for hyperspectral imaging. In *Proc. of Imaging Spectrometry of the Terrestrial Environment*, pages 173–179, 1993. 2
- [41] Katherine Salesin, Dario Seyb, Sarah Friday, and Wojciech Jarosz. Diy hyperspectral imaging via polarization-induced spectral filters. In *Proc. of International Conference on Computational Photography*, pages 1–12, 2022. 3
- [42] Cedric Scheerlinck, Nick Barnes, and Robert Mahony. Asynchronous spatial image convolutions for event cameras. *IEEE Robotics and Automation Letters*, 4(2):816–822, 2019. 3
- [43] Cedric Scheerlinck, Nick Barnes, and Robert Mahony. Continuous-time intensity estimation using event cameras. In *Proc. of Asian Conference on Computer Vision*, pages 308–324, 2019. 2
- [44] Cedric Scheerlinck, Henri Rebecq, Timo Stoffregen, Nick Barnes, Robert Mahony, and Davide Scaramuzza. CED: Color event camera dataset. In *Proc. of Computer Vision and Pattern Recognition Workshops*, 2019. 3
- [45] Zheng Shi, Xiong Dun, Haoyu Wei, Siyu Dong, Zhanshan Wang, Xinbin Cheng, Felix Heide, and Yifan Peng. Learned multi-aperture color-coded optics for snapshot hyperspectral imaging. *ACM Trans. Graph.*, 43(6), 2024. 3
- [46] Suhyun Shin, Seokjun Choi, Felix Heide, and Seung-Hwan Baek. Dispersed structured light for hyperspectral 3D imaging. In *Proc. of Computer Vision and Pattern Recognition*, pages 24997–25006, 2024. 3
- [47] Tsuyoshi Takatani, Yuzuha Ito, Ayaka Ebisu, Yinqiang Zheng, and Takahito Aoto. Event-based bispectral photometry using temporally modulated illumination. In *Proc. of Computer Vision and Pattern Recognition*, pages 15638–15647, 2021. 3
- [48] Minggui Teng, Chu Zhou, Hanyue Lou, and Boxin Shi. NEST: Neural event stack for event-based image enhancement. In *Proc. of European Conference on Computer Vision*, pages 660–676, 2022. 3
- [49] Stepan Tulyakov, Daniel Gehrig, Stamatios Georgoulis, Julius Erbach, Mathias Gehrig, Yuanyou Li, and Davide Scaramuzza. Time lens: Event-based video frame interpolation. In *Proc. of Computer Vision and Pattern Recognition*, pages 16155–16164, 2021. 3
- [50] Aziz ul Rehman and Shahzad Ahmad Qureshi. A review of the medical hyperspectral imaging systems and unmixing algorithms’ in biological tissues. *Photodiagnosis and Photodynamic Therapy*, 33:102165, 2021. 2
- [51] M Vaughan. *The Fabry-Perot interferometer: history, theory, practice and applications*. Routledge, 2017. 3
- [52] Dhruv Verma, Ian Ruffolo, David B Lindell, Kiriakos N Kutulakos, and Alex Mariakakis. ChromaFlash: Snapshot hyperspectral imaging using rolling shutter cameras. *Pro. of the ACM on Interactive, Mobile, Wearable and Ubiquitous Technologies*, 8(3):1–31, 2024. 3
- [53] Ashwin Wagadarikar, Renu John, Rebecca Willett, and David Brady. Single disperser design for coded aperture snapshot spectral imaging. *Applied Optics*, 47(10):B44–B51, 2008. 2, 3
- [54] Yibo Xu, Anthony Giljum, and Kevin F Kelly. A hyperspectral projector for simultaneous 3d spatial and hyperspectral imaging via structured illumination. *Optics Express*, 28(20):29740–29755, 2020. 3
- [55] Motoki Yako, Yoshikazu Yamaoka, Takayuki Kiyohara, Chikai Hosokawa, Akihiro Noda, Klaas Tack, Nick Spooren, Taku Hirasawa, and Atsushi Ishikawa. Video-rate hyperspectral camera based on a cmos-compatible random array of Fabry–Pérot filters. *Nature Photonics*, 17(3):218–223, 2023. 2, 3

- [56] Hui-Shyong Yeo, Juyoung Lee, Andrea Bianchi, David Harris-Birtill, and Aaron Quigley. Specam: Sensing surface color and material with the front-facing camera of a mobile device. In *Proc. of International Conference on Human-Computer Interaction with Mobile Devices and Services*, pages 1–9, 2017. [3](#)
- [57] Bohan Yu, Jieji Ren, Jin Han, Feishi Wang, Jinxiu Liang, and Boxin Shi. EventPS: Real-Time Photometric Stereo Using an Event Camera. In *Proc. of Computer Vision and Pattern Recognition*, pages 9602–9611, 2024. [3](#)
- [58] Xin Yuan. Generalized alternating projection based total variation minimization for compressive sensing. In *IEEE International Conference on Image Processing (ICIP)*, 2016. [3](#), [7](#)
- [59] Xin Yuan, David J Brady, and Aggelos K Katsaggelos. Snapshot compressive imaging: Theory, algorithms, and applications. *IEEE Signal Processing Magazine*, 38(2):65–88, 2021. [2](#)
- [60] Jingang Zhang, Runmu Su, Qiang Fu, Wenqi Ren, Felix Heide, and Yunfeng Nie. A survey on computational spectral reconstruction methods from rgb to hyperspectral imaging. *Scientific Reports*, 12(1):11905, 2022. [2](#), [3](#)

Active Hyperspectral Imaging Using an Event Camera Supplementary Material

Bohan Yu^{1,2†} Jinxiu Liang^{1,2} Zhuofeng Wang³
Bin Fan^{1,2} Art Subpa-asa⁴ Boxin Shi^{1,2*} Imari Sato⁴

¹ State Key Laboratory for Multimedia Information Processing, School of Computer Science, Peking University

² National Engineering Research Center of Visual Technology, School of Computer Science, Peking University

³ School of Electronics Engineering and Computer Science, Peking University ⁴ National Institute of Informatics

ybh1998@pku.edu.cn, cssherryliang@pku.edu.cn, wangzf2003@stu.pku.edu.cn,
binfan@pku.edu.cn, subpa@nii.ac.jp, shiboxin@pku.edu.cn, imarik@nii.ac.jp

6. More Implementation Details

6.1. More Details on Calibration

Constant light intensity calibration. We employ a smartphone display as a constant light source to provide stable baseline illumination. The absolute intensity c is measured using a calibrated radiometer. While this parameter is crucial for absolute intensity measurements, it can be adjusted arbitrarily when only relative spectral information is required, effectively serving as an exposure control parameter.

Spectral response calibration. We employ an end-to-end calibration approach for the camera’s spectral response $D(\lambda)$ using a color checker’s white region as a reference. By comparing our system’s reconstruction against ground truth measurements from a spectrometer, we derive channel-specific correction factors that compensate for both the camera’s spectral sensitivity and other systematic non-idealities in the imaging pipeline.

Event threshold calibration. The event triggering threshold C is calibrated using the color checker’s grayscale patches, utilizing their known linear intensity relationship. We perform an end-to-end calibration by adjusting the threshold value until the reconstructed intensities of the gray patches exhibit the expected linear distribution. This approach simultaneously accounts for positive and negative contrast thresholds, assuming symmetric triggering behavior.

Co-axial setup of the event camera and illumination. We place the event camera straight below the light source. This horizontal co-axial alignment ensures consistent temporal-spectral mapping, unaffected by object depth. The right picture shows that there is no horizontal cast shadow on the left or right of the rod in the front, and the rainbow is

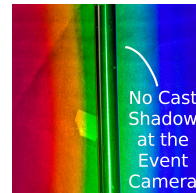


Figure 9. Co-axial setup of the event camera and illumination. The vertical rod does not cast a shadow on the background plate, indicating that the illumination and camera are placed in a horizontally co-axial.

consistent across depth changes. Vertical misalignment may cause shadows in the up and down direction, but does not affect the illumination pattern mapping accuracy. Robustness is also validated through consistent results across the video.

6.2. More Details on Hardware Configuration

As shown in Fig. 2, we employ multiple optical components to construct the “sweeping rainbow” illumination pattern. The physical device is shown in Fig. 10. The working principles of each component in our hyperspectral imaging system are as follows (in light path order):

- **Point light source: Initial illumination.** A xenon arc lamp (Asahi Spectra MAX-303) provides wide, flat spectrum distribution across the visible range, ensuring complete spectral sampling. Its high-intensity output enables reliable event triggering in the camera. The continuous nature of its spectrum is essential for capturing the full range of spectral information without gaps.
- **First convex lens: Concentration.** The first convex lens with a 50mm focal concentrates the light onto a controllable-width slit to maximize light efficiency, a critical factor given the system’s need for sufficient intensity to trigger events.
- **Vertical slit: Width control.** The vertical slit with con-

*Corresponding author: Boxin Shi

†This work was conducted while the first author, Bohan Yu, was doing internship at National Institute of Informatics.

trollable width controls the spatial width of the light beam, which directly influences the final spectrum’s FWHM.

- **Second convex lens: Collimation.** The second convex lens with a 50mm focal transforms the divergent light into parallel rays. This collimation is essential for optimal interaction with the blazed grating, as parallel light ensures consistent diffraction angles across the beam width.
- **Cylindrical convex lens: Shape control.** The cylindrical convex lens with 150mm focal converges the light vertically at the spinning mirror to minimize the required mirror size and then allows the light to diverge vertically, creating the characteristic tall rainbow strip pattern. It optimizes beam shape for efficient scanning.
- **Blazed grating: Spectral separation.** The blazed grating with 600 lines/mm is used for spectral separation. This precise spacing is optimized for visible light diffraction, horizontally dispersing different wavelengths while maintaining high diffraction efficiency. The grating reflects this spectrally separated light toward the mirror array.
- **Rotated mirror array: Temporal scanning.** The four-mirror array driven by a stepper motor and gear system reflects the rainbow strip pattern and sweeps it across the scene in a horizontal pattern. The system achieves rotation speeds up to 1800 revolutions per minute (rpm), enabling rapid spectral scanning while maintaining sufficient dwell time for event generation at each wavelength.

All optical elements are mounted on a vibration-isolated optical breadboard. These components create a precise and efficient spectral scanning system. As to the positions of optical components, 4 of 5 DoFs are fixed for light passing straight through the center. The distances between them are then tuned for maximum brightness at the slit (first lens), narrow output rainbow spectra (second lens), and appropriate 1st-order diffraction within the mirror range (grating). The small diffraction area of the grating ($< 2\text{cm}$) allows approximating light as a point source at the grating’s image in the mirror. Each element’s parameters have been optimized to balance competing requirements: spectral resolution, light efficiency, scanning speed, and system compactness. The result is a system capable of real-time hyperspectral imaging while maintaining the bandwidth efficiency inherent to event-based sensing.

6.3. More Details on Algorithm Configuration

The computational pipeline of the proposed method is built on a hybrid architecture that leverages both CPU and GPU resources. Event pre-processing is accelerated using Numba just-in-time compilation, while the reconstruction algorithms are implemented in PyTorch to utilize GPU parallelization. The experiments are conducted on a single NVIDIA GeForce RTX 3060 graphics card. It takes about 20 seconds to reconstruct a hyper-spectral frame. For visualization purposes, we employ a color space conversion pipeline that transforms

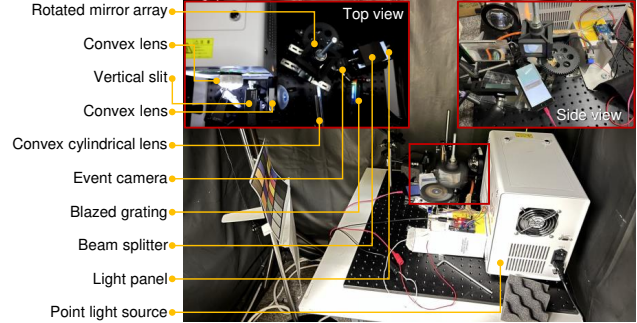


Figure 10. System prototype (corresponding to Fig. 1(a)).

the reconstructed hyperspectral data through CIE 1931 color space before final conversion to RGB using OpenCV’s color management system.

6.4. More Details on Data simulation

Our synthetic dataset generation pipeline simulates the complete optical and sensing characteristics of the system, including the non-ideal narrow-band illumination pattern, non-ideal event triggering, and frame camera imaging noises. The sweeping rainbow effect is modeled using narrow-band illumination with a FWHM of 17.5 nm, convolved with ground truth hyperspectral images to generate 1200 intensity frames. To achieve realistic event generation, we maintain a baseline illumination at 3% of the maximum scene intensity. The event camera’s behavior is carefully modeled with triggering thresholds C following a normal distribution with mean 0.15 and standard deviation 0.01 and incorporating a 50 μs refractory period at a simulated scanning speed of 1800 rpm. During reconstruction, we employ consistent parameter settings with regularization weight $\alpha_{\text{int}} = 1.0$ and M_{start} of $0.3 \times M$. For the frame-based camera, we designed equivalent capture scenarios that match our system’s operating conditions. The frame-based synthetic data incorporates multiplicative white Gaussian noise with a standard deviation of 0.067 to match the noise characteristics of event cameras.

6.5. More Details on Compared methods

We evaluate the proposed system against the following baselines:

- **Full-bandwidth frame-based method.** The frame-based variant with full bandwidth is used for reference, which involves 1200 intensity frames with maximum temporal resolution and highest data bandwidth. Note that, for real-time capture, a high-speed camera over 3,000 FPS is required for the real scenes.
- **Bandwidth-matched frame-based method.** To ensure fair bandwidth comparisons, we account for the 16-bit event data format (assuming that the input event streams employ 16-bit Prophesee EVT 3.0 format) versus 8-bit

grayscale frames, allowing us to determine equivalent frame counts for matched-bandwidth scenarios. The reduced-bandwidth comparisons employ uniformly down-sampled frame sequences with linear interpolation for spectral reconstruction.

- **Parkkinen basis method [38].** To evaluate against basis-based methods, we implemented the Parkkinen basis [38] approach as a representative state-of-the-art technique. Ground truth hyperspectral data is first decomposed using least-squares fitting to the Parkkinen basis functions, followed by reconstruction for comparison with our method. This offers insights into the advantages of our approach for capturing narrow-band spectral features, which is difficult to achieve with basis-based methods.
- **CASSI-based method [25, 58].** To evaluate against CASSI-based methods, we simulate CASSI optical system and evaluate on two state-of-the-art techniques [25, 58].

7. More Analysis

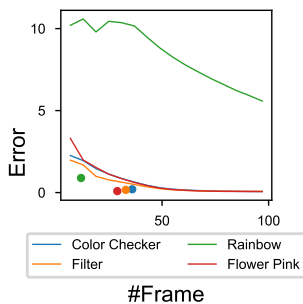


Figure 11. Comparison between frame-based method using different numbers of frames (curves) and ours (solid points) for different samples.

7.1. Bandwidth efficiency

Fig. 11 presents a comprehensive comparison of reconstruction accuracy versus data bandwidth across different methods. Our event-based approach consistently achieves superior spectral reconstruction quality compared to frame-based methods operating at equivalent bandwidth levels. Notably, our method requires only 40.47% of the bandwidth of traditional frame-based approaches to achieve comparable accuracy.

7.2. System parameters

Our detailed analysis of the relationship between planar constant light source intensity, event camera triggering threshold, and data rates reveals important system characteristics. Using a standard 24-patch color checker as our test target, we conducted comprehensive measurements across varying operating conditions. The results in Fig. 12 show that lower

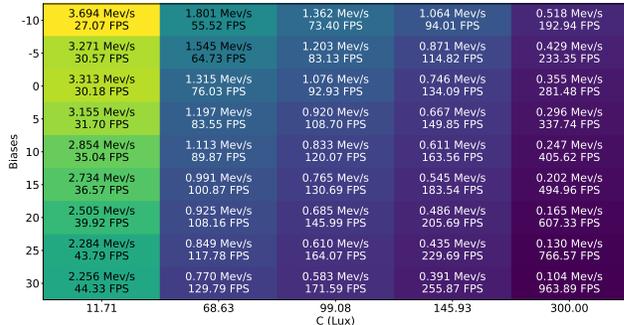


Figure 12. The analysis demonstrates the relationship between light source intensity, event camera bias settings (threshold), and data rates, thereby illustrating how system parameters can be optimized for different operating conditions and bandwidth requirements.

constant light intensities result in higher bandwidth per revolution. For the event triggering threshold, a lower threshold results in higher bandwidth per revolution. Because the Prophesee EVK4 IMX636 event camera we are using has 80 Mev/s maximum event triggering, we also calculate the theoretical maximum FPS for each setup. The final maximum FPS is also limited by the mechanical maximum rotation speed, which is 30 FPS for our current device.

Ours	DESCI [25]	GAPTV [58]
6.65	5.80	7.30

Table 1. Comparison with CASSI-based methods. Quantitative results with real and fake flowers.

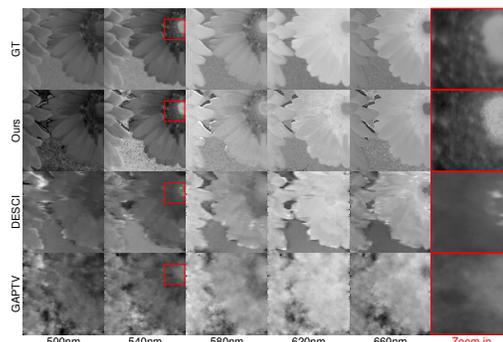


Figure 13. Comparison with CASSI-based methods. Qualitative results with real and fake flowers.

7.3. Comparison with CASSI-based methods

CASSI methods often exhibit horizontal artifacts due to the spectral-spatial encoding. Comparisons with representative CASSI methods DESCI [25] and GAPTV [58] are shown in Figure 13, with their SAM scores in Table 1. Our method leverages high temporal resolution and low bandwidth properties of event cameras and constructs spectral-temporal

encoding, avoiding cross-pixel artifacts.

8. More Results

We provide comprehensive hyperspectral reconstruction results that extend beyond the examples presented in the main text. The wavelength labels of the narrow-band images, like ‘380nm’, indicate the beginning of the spectral range.

Comparison results. In Fig. 5 of the main text, we evaluate our method’s capability to recover high-frequency spectral features of the vertical rainbow produced by the prism, comparing with ground truth, basis-based method, bandwidth-matched frame-based method. The corresponding full hyperspectral reconstruction results of different methods are shown in Fig. 14.

Results on static scenes. We include additional four examples on static scenes in Figs. 16 to 19, which contains hyperspectral reconstruction results on white daisies, yellow daisies, pink roses, and yellow roses, respectively. These examples highlight our system’s ability to distinguish between subtle spectral signatures that appear identical to the human eye.

Results on dynamic scenes. For dynamic scenes, we present the full hyperspectral reconstruction results of the iridescent sticker paper under varying viewing angles in Fig. 20 corresponding to Fig. 8 in the main text. We also present additional two new examples in Figs. 21 and 22, which show results on a deforming colorful soft toy under manual manipulation, and a compact disc exhibiting varying spectral responses across its reflection strip, respectively.

Video results. We also provide a supplementary video to demonstrate the complete workflow of our system, from hardware setup to real-time reconstruction. It includes detailed visualization of the “sweeping rainbow” effect, event generation patterns, and reconstruction results. The video also shows real-time visualizations of our three dynamic scenes shown in Figs. 20 to 22, effectively illustrating the system’s capability to capture rapid spectral variations. The video also serves to validate our claims regarding temporal resolution and system responsiveness under real-world conditions.



Figure 14. The full hyperspectral reconstruction results for examples in Fig. 5. Comparative analysis of spectral reconstruction on a high-frequency rainbow pattern. Compared methods include (a) ground truth, (b) ours, (c) basis-based method, and (d) bandwidth-matched frame-based method.

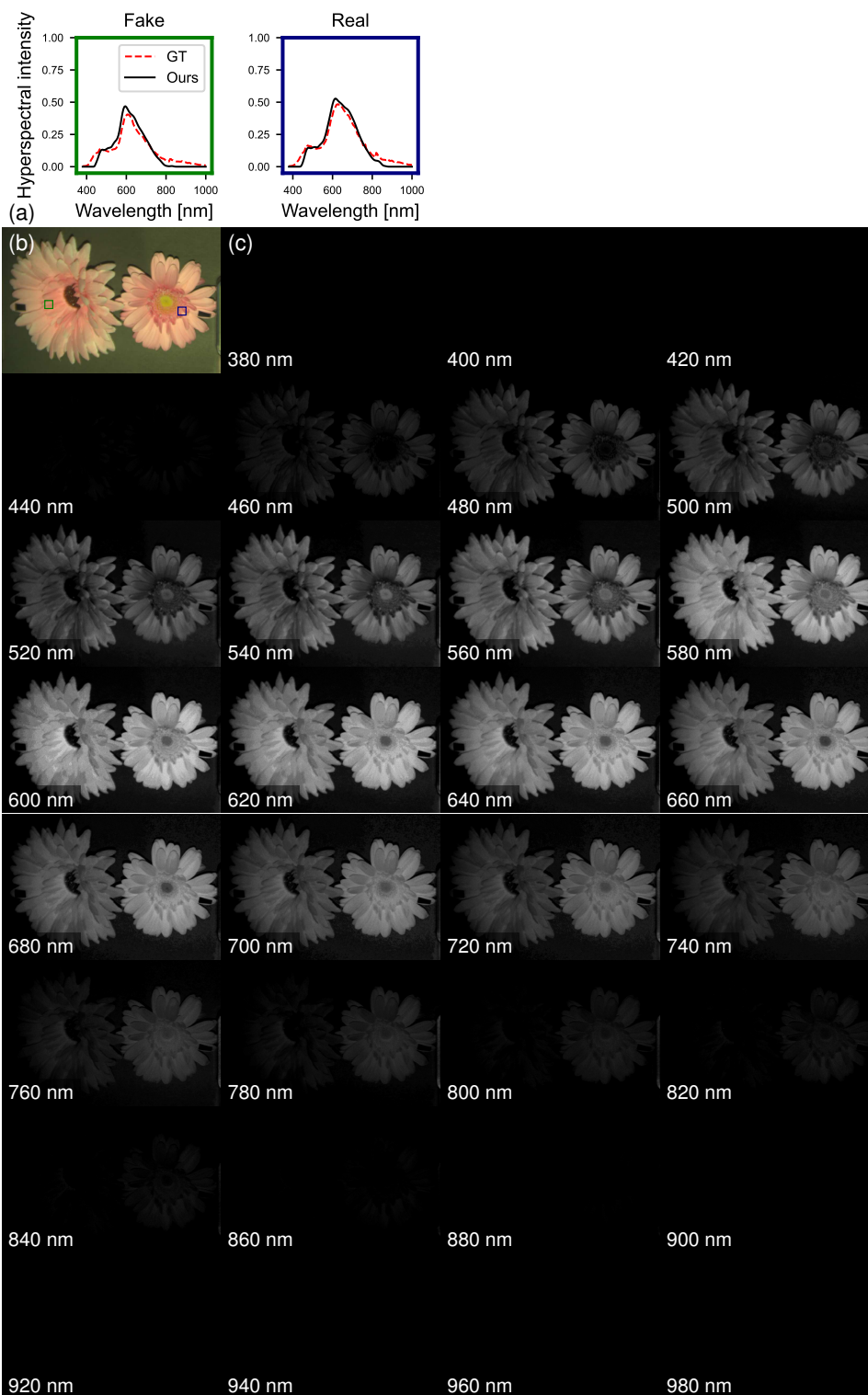


Figure 15. The full hyperspectral reconstruction results for samples in Fig. 7. (a) Spectra of metamer samples against ground truth measurements, highlighting the system’s ability to capture subtle spectral differences. (b) The reconstructed hyperspectral image in sRGB. (c) Estimated hyperspectral images.



Figure 16. Evaluation of metamer samples of real (left) and fake (right) white daisies. (a) Spectra of metamer samples against ground truth measurements, highlighting the system's ability to capture subtle spectral differences. (b) The reconstructed hyperspectral image in sRGB. (c) Estimated hyperspectral images.

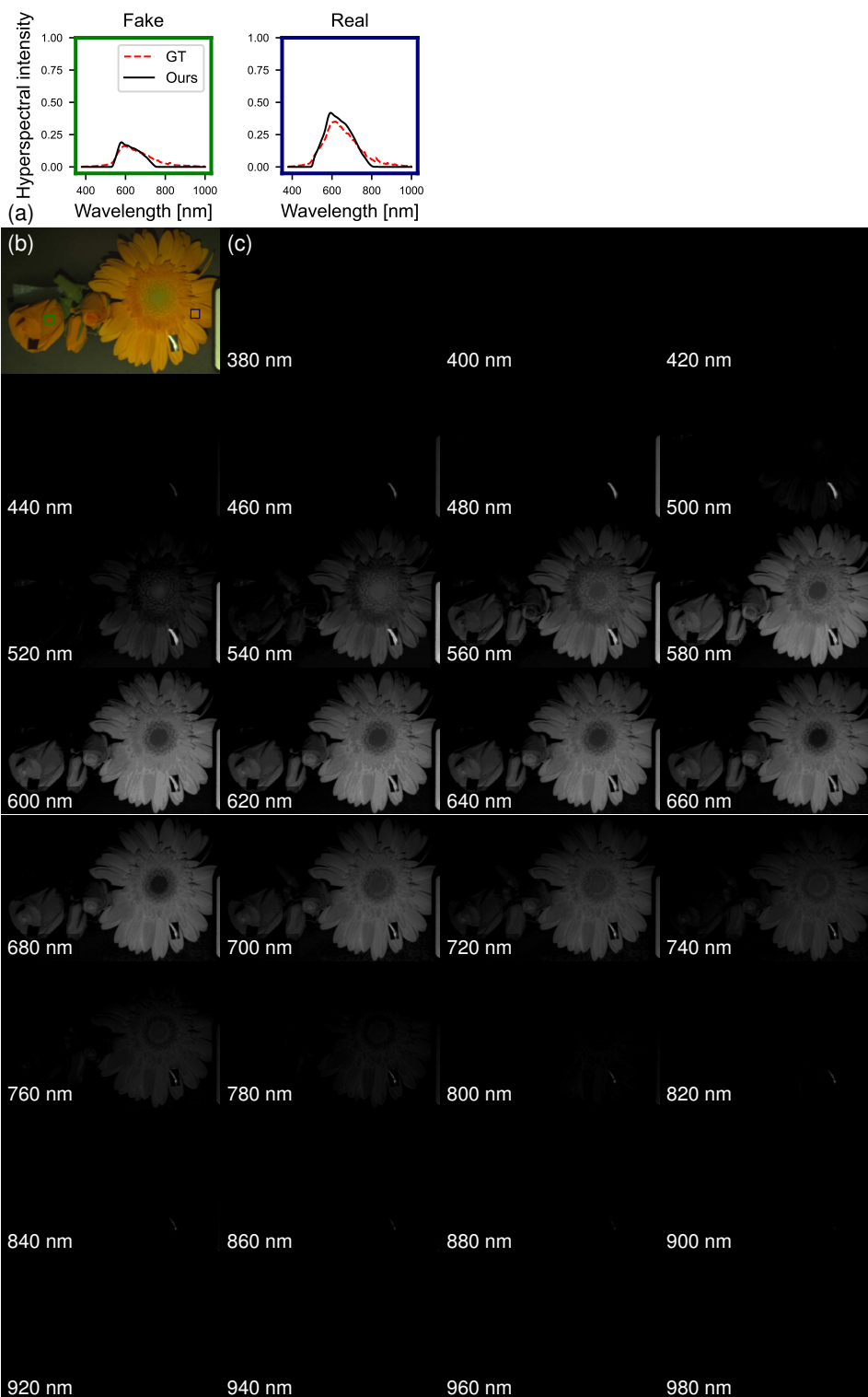


Figure 17. Evaluation of metameric samples of yellow rose (left) and daisy (right). (a) Spectra of metameric samples against ground truth measurements, highlighting the system’s ability to capture subtle spectral differences. (b) The reconstructed hyperspectral image in sRGB. (c) Estimated hyperspectral images.

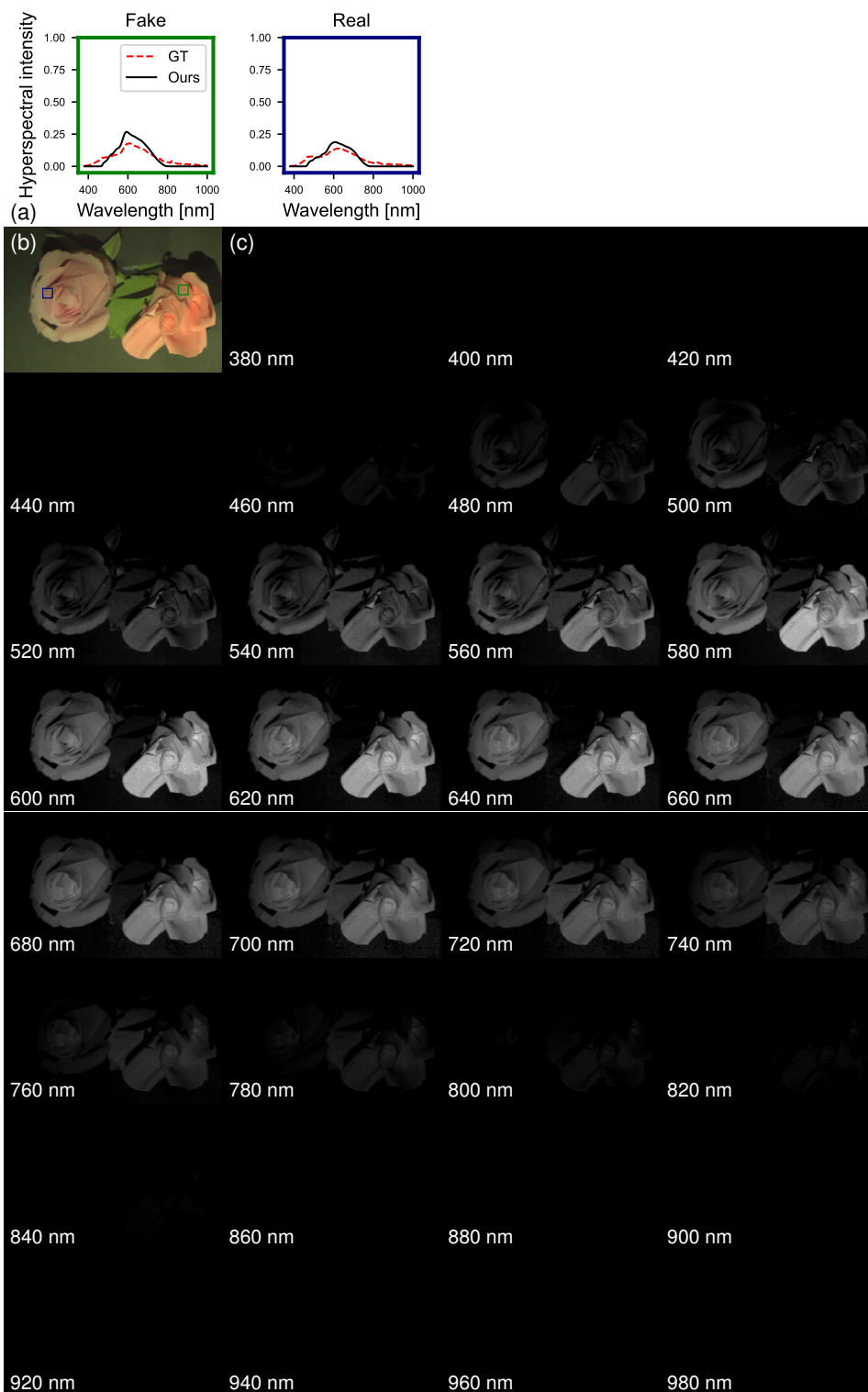


Figure 18. Evaluation of metamer samples of real (left) and fake (right) pink roses. (a) Spectra of metamer samples against ground truth measurements, highlighting the system’s ability to capture subtle spectral differences. (b) The reconstructed hyperspectral image in sRGB. (c) Estimated hyperspectral images.

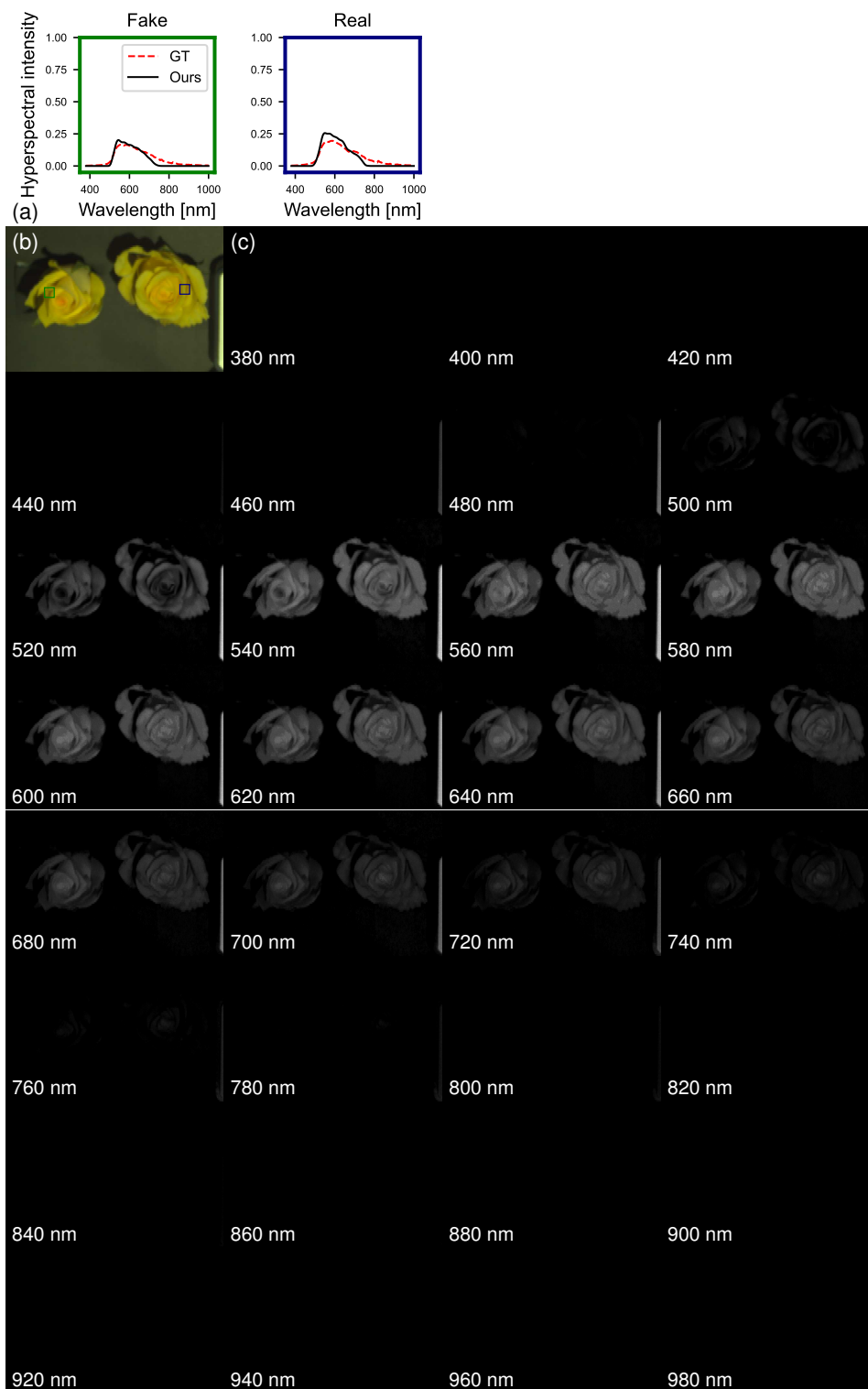


Figure 19. Evaluation of metamer samples of fake (left) and real (right) yellow roses. (a) Spectra of metamer samples against ground truth measurements, highlighting the system's ability to capture subtle spectral differences. (b) The reconstructed hyperspectral image in sRGB. (c) Estimated hyperspectral images.

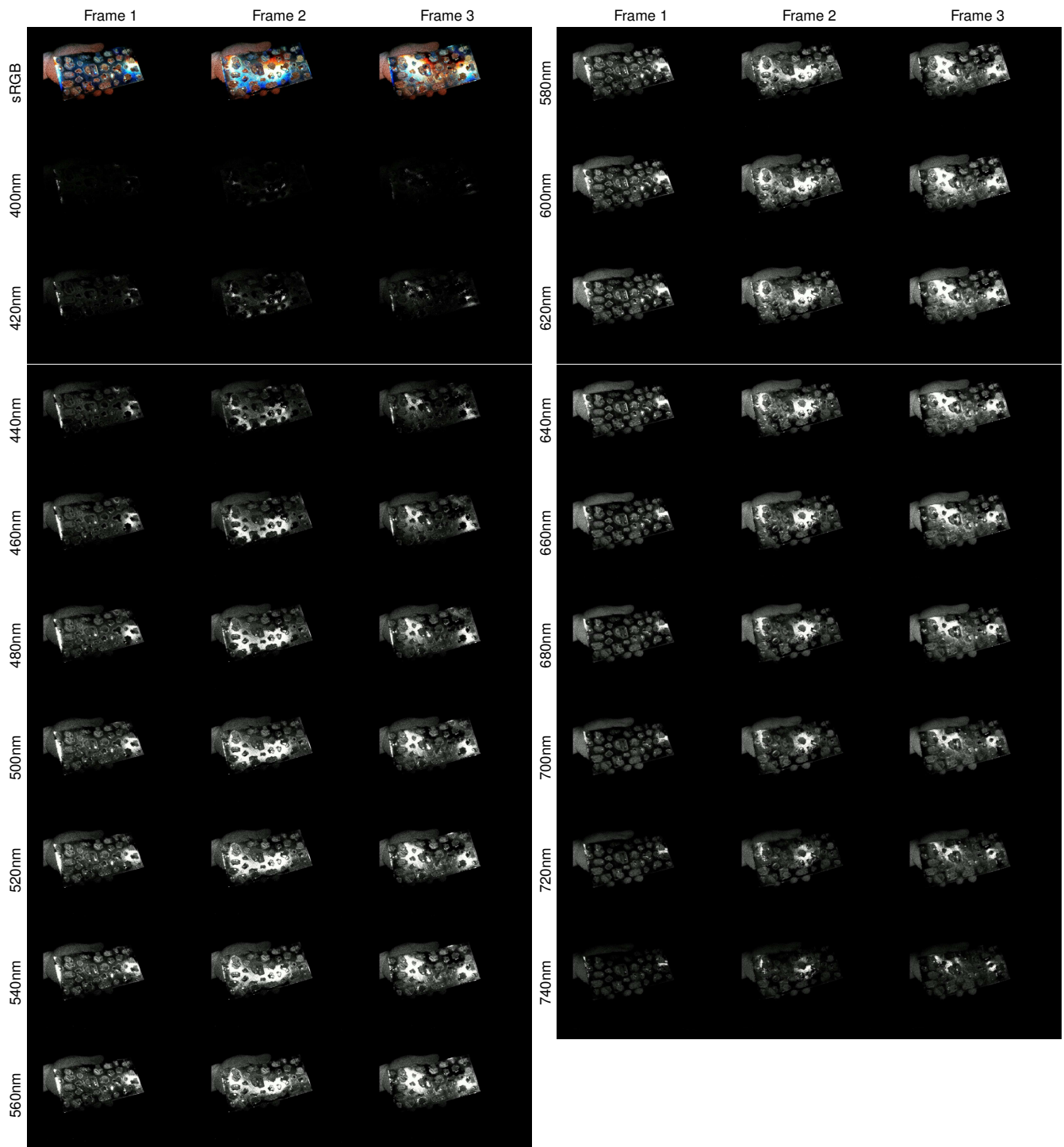


Figure 20. Real-time hyperspectral imaging on a moving iridescent sticker paper. Top-left: Three consecutive estimated hyperspectral images rendered in sRGB. Remaining panels: Corresponding estimated hyperspectral images (380-780nm, sampled at 20nm intervals).

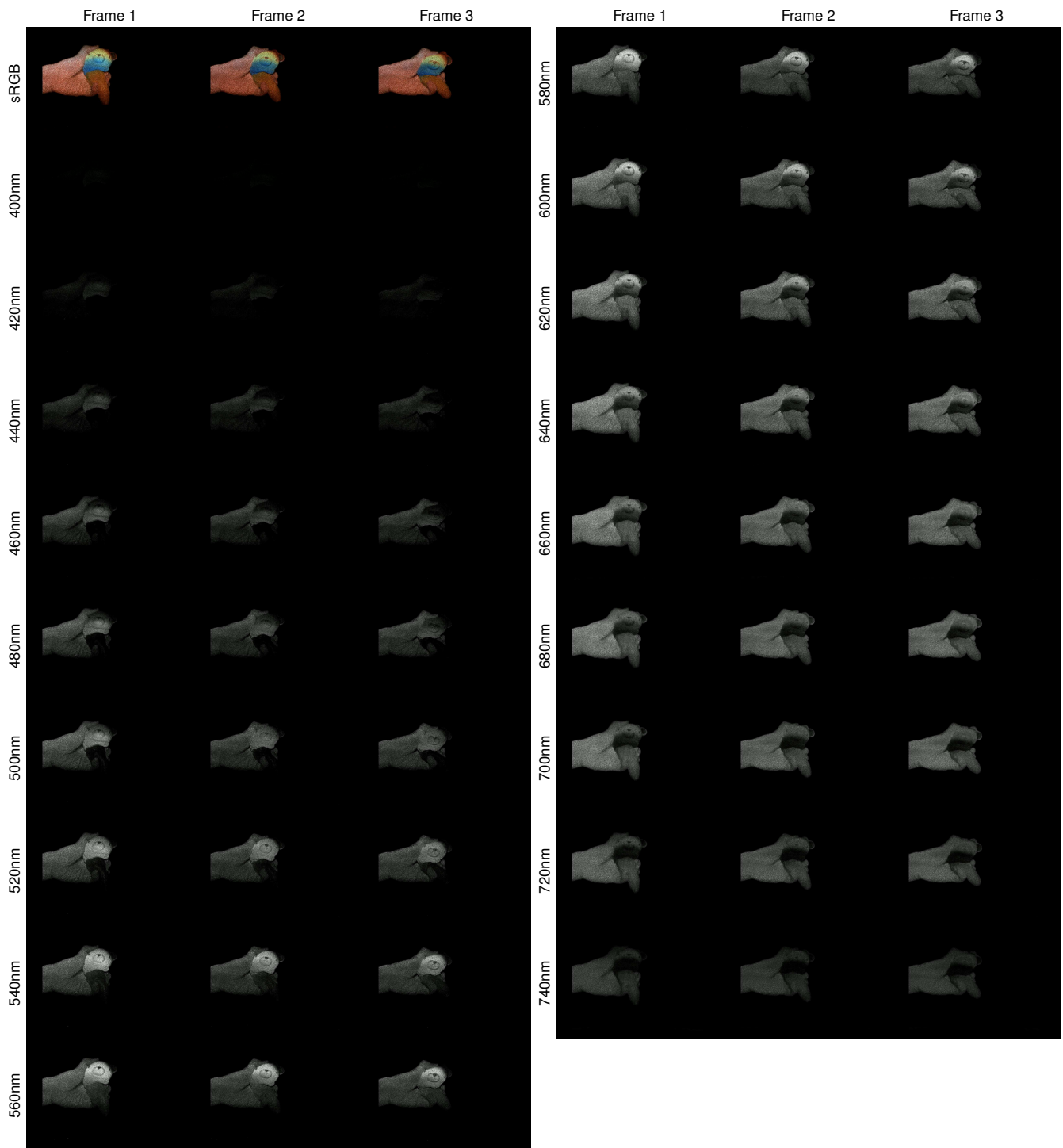


Figure 21. Real-time hyperspectral imaging on a deforming colorful soft toy under manual manipulation. Top-left: Three consecutive estimated hyperspectral images rendered in sRGB. Remaining panels: Corresponding estimated hyperspectral images (380-780nm, sampled at 20nm intervals).

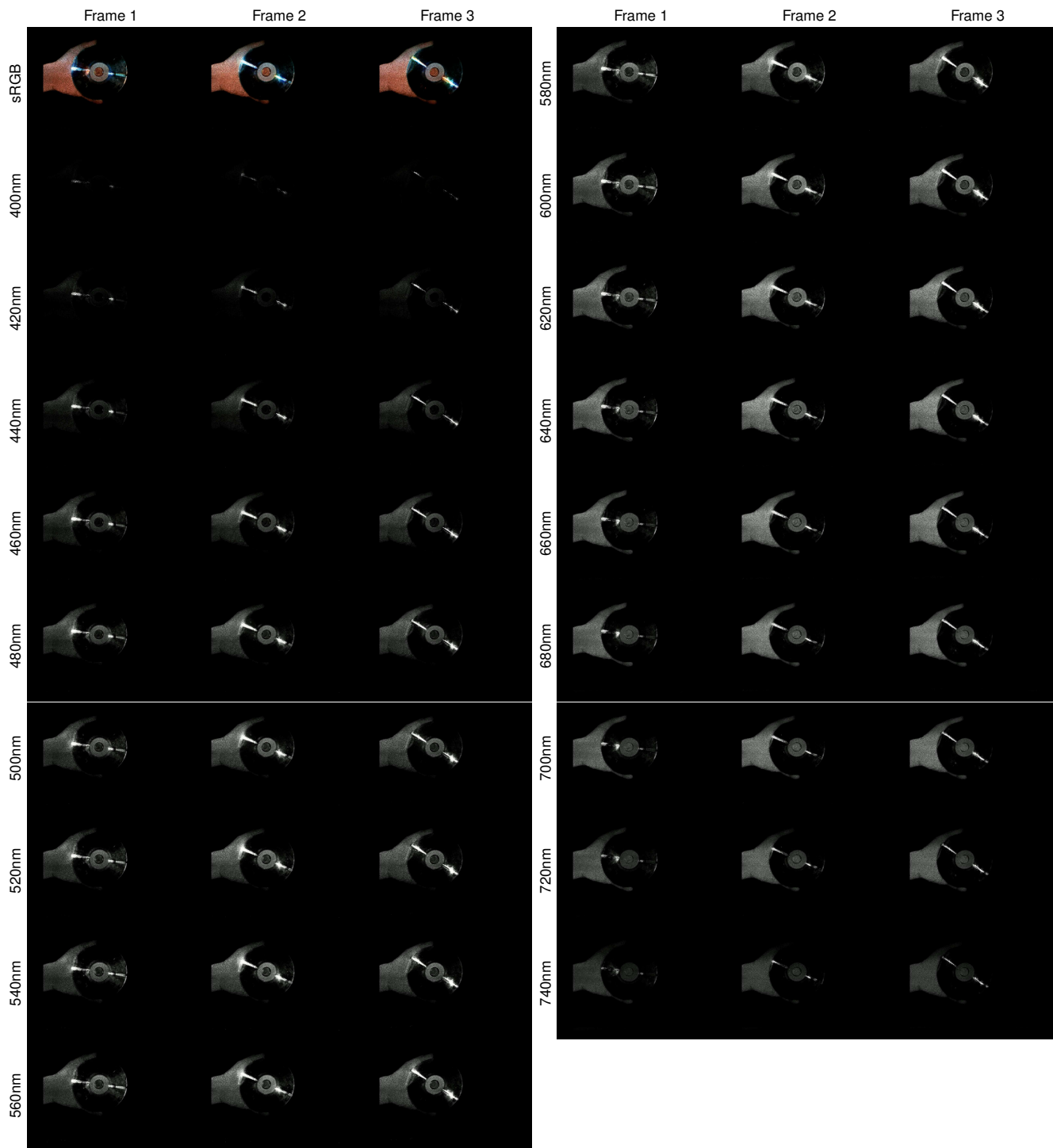


Figure 22. Real-time hyperspectral imaging on a compact disc exhibiting varying spectral responses across its reflection strip. Top-left: Three consecutive estimated hyperspectral images rendered in sRGB. Remaining panels: Corresponding estimated hyperspectral images (380-780nm, sampled at 20nm intervals).